

## Assessing the Reproducibility of IN718 Parts on Similar L-PBF Systems Through Mechanical Properties and Dimensional Accuracy

Mikyle Paul<sup>1,2</sup>, Indrajit Nandi<sup>1,2</sup>, Shuai Shao<sup>1,2</sup>, Nima Shamsaei<sup>1,2\*</sup>

<sup>1</sup> *Department of Mechanical Engineering, Auburn University, Auburn, AL 36849, USA*

<sup>2</sup> *National Centre for Additive Manufacturing Excellence (NCAME), Auburn University, Auburn,  
AL 36849, USA*

\* Corresponding author:

Email: [shamsaei@auburn.edu](mailto:shamsaei@auburn.edu)

Tel: (334) 844 4839

### **Abstract**

Reproducing parts of equal quality on different additive manufacturing (AM) machines, particularly laser powder bed fusion systems, can prove to be challenging due to the numerous process variables affecting final part quality. Original equipment manufacturers (OEMs) recommend regular system calibration to minimize the differences in part quality. Current efforts are going towards process qualification and standardization to ensure that parts of equal quality can be fabricated regardless of where they are fabricated. As such, this study aims to assess the reproducibility of IN718 parts fabricated on three EOS M290 machines by comparing mechanical properties, including tensile and fatigue, and dimensional accuracy. Results showed minor differences in strength and ductility, and subtle differences in fatigue life. These differences could relate to inconsistencies in heat treatment between fabrication sites inducing different microstructures. Dimensional accuracy was unaffected and therefore reproducible among the three machines.

**Keywords:** Laser powder bed fusion (L-PBF/LB-PBF), IN718, Equivalency, Micro-/defect-structure, Mechanical behavior, Dimensional accuracy

## **Introduction**

Additive manufacturing (AM) is a promising technique for fabricating near-net-shape parts [1,2]. Several types of AM techniques exist with laser powder bed fusion (L-PBF) being a popular one due to its ability to produce parts with high geometric accuracy [3]. Laser powder bed fusion has therefore been adopted by various industries including biomedical, aerospace, and automotive [4,5]. Some of the challenges associated with L-PBF, however, are process induced volumetric defects, microstructural anisotropy, and residual stresses [6,7]. Due to the numerous process variables involved during fabrication, slight variations in them due to factors such as machine health, feedstock, and machine setup can lead to differences in final part quality [8]. Ensuring that parts are repeatable on the same machine and reproducible on similar machines with different serial numbers is critical for the success of industrial applications of L-PBF. As a result, original equipment manufacturers (OEMs) suggest regular maintenance on machines to ensure that all systems are operating as designed.

Apart from regular maintenance, standards organizations are working with OEMs to standardize L-PBF (among other AM processes) to ensure quality control and traceability of all manufactured components. Process qualification is one of the steps in standardization and is crucial for implementing L-PBF in critical applications [9]. Qualification principles as outlined in ISO/ASTM 52930 [10] consist of three sectors including installation qualification (IQ), operation qualification (OQ), and performance qualification (PQ). In simple terms, IQ ensures that the machine has been installed correctly; OQ ensures that the machine can consistently produce parts of acceptable quality; PQ ensures that the product specifications are met through process monitoring systems or other regulatory checks. These qualification principles in conjunction with quality management systems have been developed to manage the quality of L-PBF parts and to ensure that they meet the minimum requirements set by OEMs and standards organizations.

Considering the steps associated with process qualification, some of the key factors that need to be taken into consideration include feedstock quality, machine setup, process parameter selection, and characterization technique. Ensuring that all these factors are identical across builds on similar L-PBF systems with different serial numbers may be challenging. For example, if machines are in different parts of the world, access to the same quality of feedstock, process gas, and characterization techniques may be difficult especially for “point-of-need” applications. Additionally, ambient conditions may be completely different resulting in dissimilar loads on ancillary equipment affecting key process variables during fabrication, i.e., hot versus cold environments. Although machines may be nominally identical, variations in any of the abovementioned factors during fabrication may affect micro-/defect-structures, mechanical properties including tensile and fatigue, and dimensional accuracy [11]. For components required in critical load bearing applications, mechanical performance cannot be compromised. Furthermore, for parts requiring fine tolerances, dimensional accuracy of fabricated parts is imperative.

Therefore, this study aims to investigate the reproducibility of parts fabricated on three nominally identical L-PBF machines with different serial numbers by evaluating their tensile and fatigue behavior as well as dimensional accuracy. Inconel 718 (IN718) has been used in this study due to its applicability in various industrial sectors such as aerospace and power generation [12,13]. The qualification principles mentioned above were applied to each build to ensure uniformity and allow for traceability of any issues or inconsistencies encountered along the way.

### Experimental procedures

Three builds were conducted on each of three EOS M290 L-PBF systems denoted as Machine 1, Machine 2, and Machine 3, using identical build layouts as depicted in Figure 1. Process parameters recommended by EOS for IN718 were used for this study including a laser power of 285 W, scanning speed of 960 mm/s, hatching distance of 0.11 mm, and layer thickness of 0.04 mm. To ensure the success of each build, a carbon fiber brush recoater was used. Fabrication with Machine 1 used IN718 plasma atomized powder supplied by AP&C and fabrication with Machines 2 and 3 used powder supplied by Sandvik. Each powder lot had a particle size distribution in the range of 15 – 53  $\mu\text{m}$ , however, the AP&C powder had undergone six reuses prior whereas the Sandvik powder was virgin. Figure 1 includes various parts that were used for different tests, inspections, and characterizations.

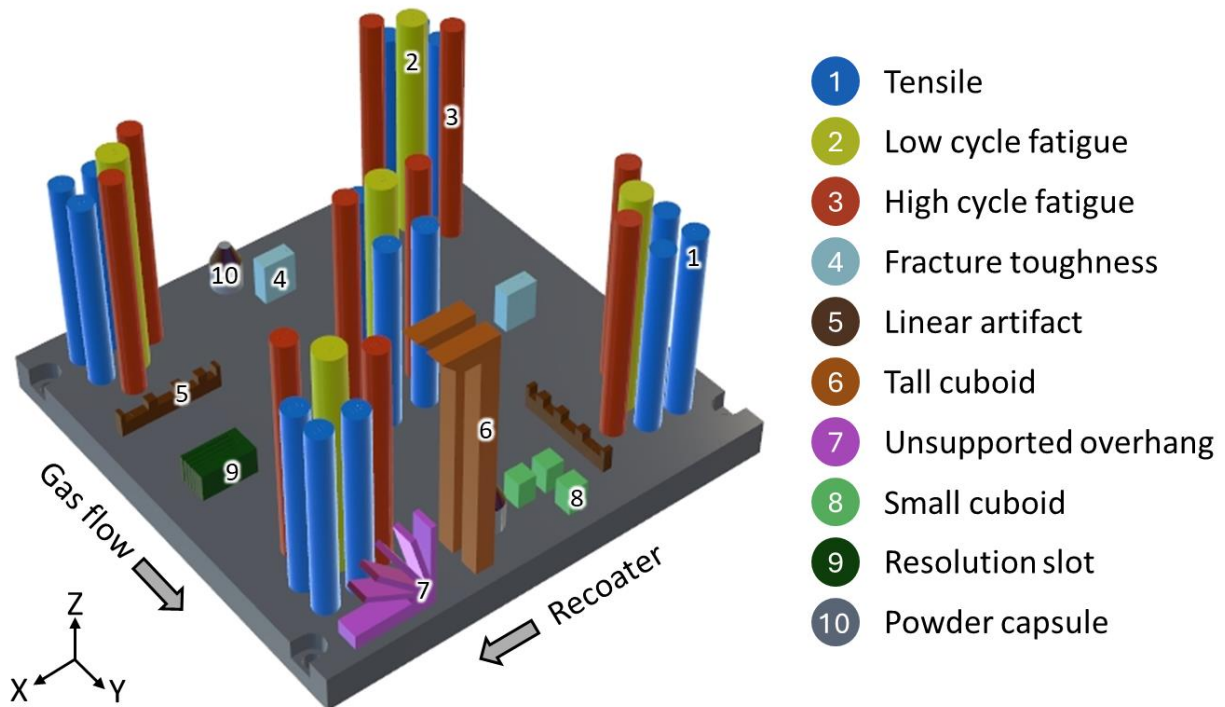


Figure 1: Build layout for IN718 parts.

The parts located towards the south side of the build plate, i.e., near the gas extraction nozzle, were strategically placed to allow for removal after fabrication using a wire electro-

discharge machine (EDM) to observe the as-built microstructure. This included the unsupported overhang, one of the tall cuboids, and one of the small cuboids. Additionally, the powder capsules, which were fabricated on supports, were removed to undergo chemical composition and particle size distribution analyses using inductively coupled plasma mass spectroscopy and laser diffraction, respectively. After removal of these parts, each build plate underwent stress relief (SR) at 1065 °C for 1.5 hours. Thereafter, all parts were detached from the build plate using a wire EDM. Following removal, all parts underwent hot isostatic pressing (HIP), solution annealing (SA), and double aging. The full heat treatment (HT) schedule can be observed in Table 1.

*Table 1: Heat treatment schedule applied to all applicable parts.*

<b>Stress Relief (SR)</b>	<b>Hot Isostatic Pressing (HIP)</b>	<b>Solution Annealing (SA)</b>	<b>1<sup>st</sup> Step Aging</b>	<b>2<sup>nd</sup> Step Aging</b>
1065 °C/1.5 h	1162 °C/3.5 h/100 MPa	1065 °C/1 h	760 °C/10 h	650 °C/10 h

Mechanical behavior was assessed through tensile, low cycle fatigue (LCF), and high cycle fatigue (HCF) tests (geometries included in Figure 2a) and b), respectively). Fracture toughness specimens were fabricated however they were not used in this study. Both tensile and fatigue tests were conducted on servo-hydraulic load frames. Tensile tests were conducted in strain-controlled mode at a strain rate of 0.005 mm/mm/min according to ASTM E8 [14]. Low cycle fatigue tests were also strain-controlled and were fully reversed ( $R = -1$ ) with a strain amplitude of 0.005 mm/mm at a frequency of 0.5 Hz following a sinusoidal waveform according to ASTM E606 [15]. High cycle fatigue tests were performed under tension-tension loading ( $R = 0.1$ ) and in load controlled mode also following a sinusoidal waveform according to ASTM E466 [16]. Maximum stresses for HCF tests ranged from 875 to 600 MPa to obtain an more complete S-N relation. Fractography on selected tensile and fatigue specimens was conducted using a Zeiss Crossbeam 550 scanning electron microscope (SEM).

Microstructure was assessed on the XY and XZ-planes of tall and small cuboids for the as-built and heat-treated (HT) conditions. Coupons were prepared for metallography by sectioning, mounting in epoxy, grinding using progressively finer sandpapers (ranging from 280 to 1000 grits), and polishing using a ChemoMet pad and 0.05  $\mu\text{m}$  colloidal silica to obtain a mirror finish. The abovementioned SEM was used in conjunction with an electron backscattered diffraction (EBSD) detector from Oxford Instruments to analyze the microstructure of coupons from Machine 1. As-built coupons from Machines 2 and 3 were etched using Kalling's reagent and analyzed using an optical microscope whereas HT ones were analyzed on backscattered electron (BSE) images obtained from the SEM. Porosity was represented by relative density and was measured on the same as-built and HT coupons using an optical method.

Dimensional accuracy and feature resolution were assessed through the linear artifact, resolution slot, and unsupported overhang. The geometries for the various artifacts have been

included in Figure 2c) – e). Measurements on the linear artifact and resolution slot were reported as recommended in ISO/ASTM 52902 [17]. Linear artifacts from Machine 1 were measured using calipers whereas the ones from Machines 2 and 3 were measured using a coordinate measuring machine (CMM). Resolutions slots underwent a go/no-go check using feeler gages for all three machines. For the unsupported overhang, the surface roughness of the downskin surfaces of each overhang were measured using an optical method for Machine 1 and a contact profilometer for Machine 2 and 3.

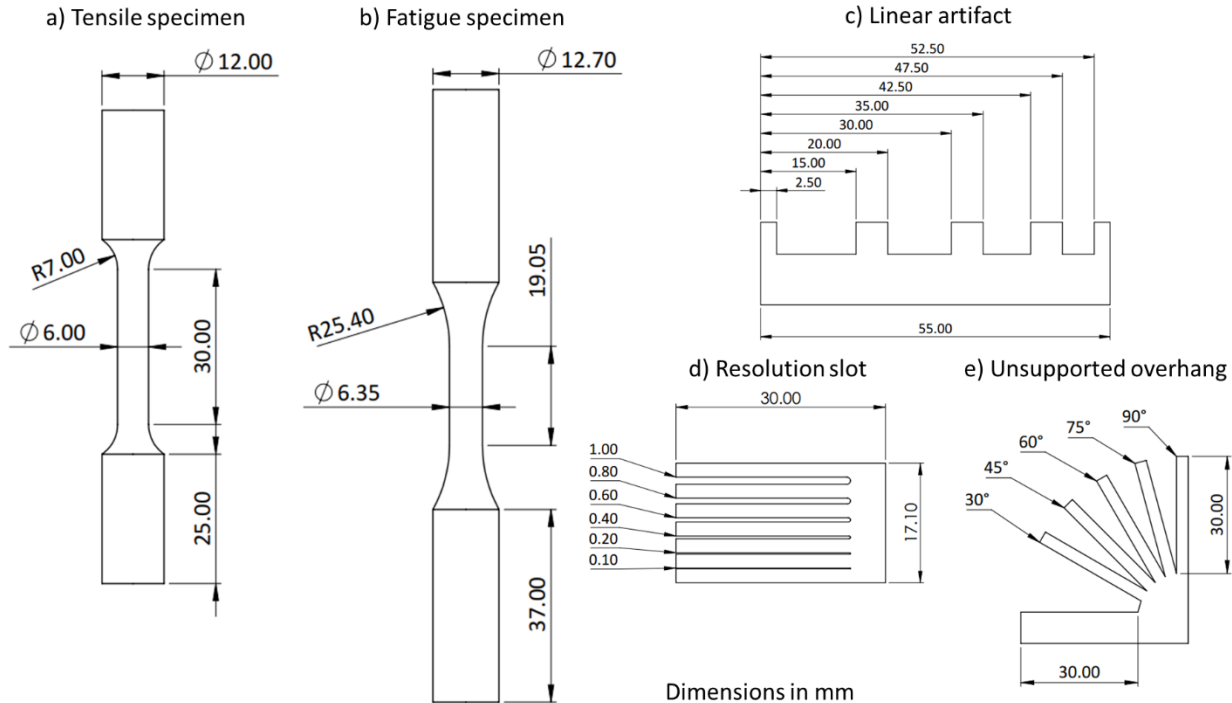


Figure 2: Geometries for various test specimens and artifacts.

## **Results and discussion**

Dimensional accuracy and part resolution were evaluated for different machines using different geometric artifacts and measurement techniques. Firstly, linear positioning accuracy was evaluated with the use of two linear artifacts oriented along the X and Y directions. The deviations from the nominal design values have been plotted in Figure 3. In general, Machine 1 dimensions can be observed to be slightly below the nominal values in both the X and Y directions. Machine 2 dimensions in the X direction can be observed to be above the nominal values whereas the Y direction appears to be quite close to the nominal. Machine 3 dimensions show more consistency than the other machines with slightly lower values than the nominal in some cases. The measured deviation is compounded further away from the datum. Machine 1 dimensions were measured using a calibrated caliper with an accuracy of  $\pm 0.02$  mm. Although multiple measurements were taken and averaged, user error may have affected the measurements resulting in slightly inaccurate readings when compared to those measured with the use of CMM. Although CMM was used for

both Machines 2 and 3, the measurements still vary from the nominal, especially for Machine 2. A possible explanation for these deviations may be the offset and scaling values input into the build file. EOS M290 machines require a “fine tune” build to be conducted that is used as a calibration to offset the laser beam for a specific material and process parameter set, as well as to create compensations in the X and Y scaling to ensure geometric accuracy is maintained. If these values were not correctly input into the build file due to operator or measurement error, it may result in the observed differences.

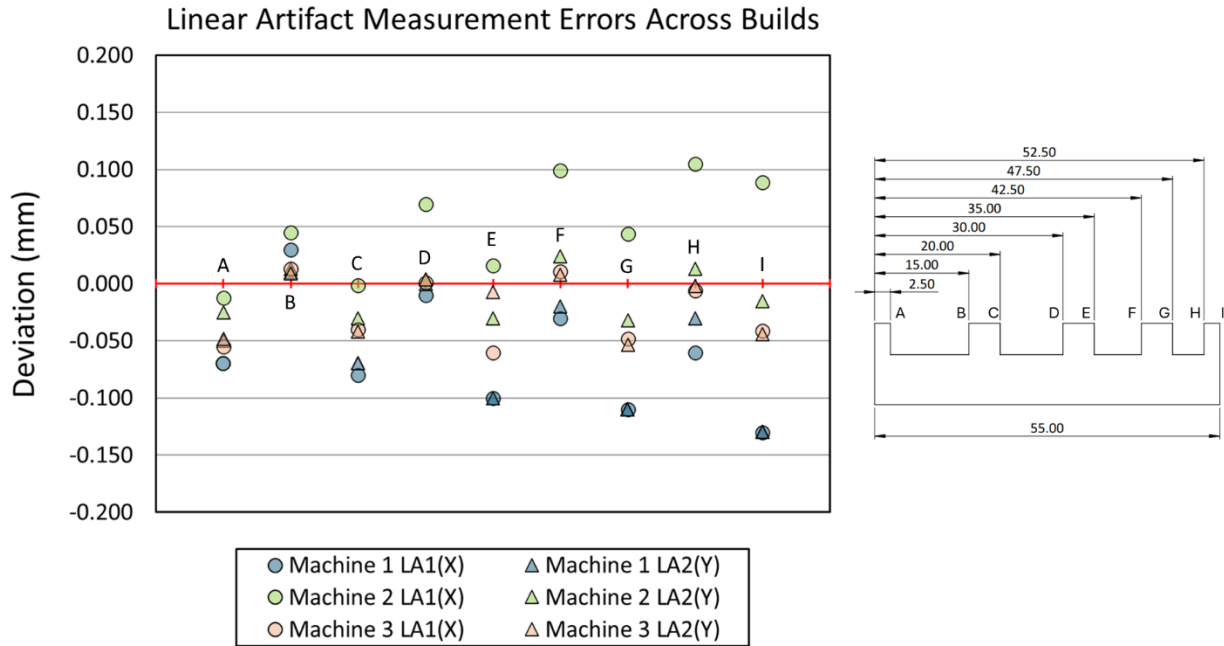


Figure 3: Linear artifact dimensions in two directions for all three machines.

The resolution slot allows for determination of the minimum slot width that can be fabricated on an L-PBF system along with the accuracy of fabricated slots. For this, feeler gages were used to determine each slot width. The reported slot width corresponds to the thickest feeler gage that was able to pass through the slot. All machines show comparable measurements. In general, Machine 1 slots tended to be slightly undersized compared to the others. Slots were measured after SR and it was observed that some powder particles were impinged on the internal surfaces of the Machine 1 slot effectively decreasing the overall slot width. This could be as a result of inadequate powder removal during the depowdering stage. Lastly, for the narrowest slot (0.1 mm), no feeler gage was able to pass through.

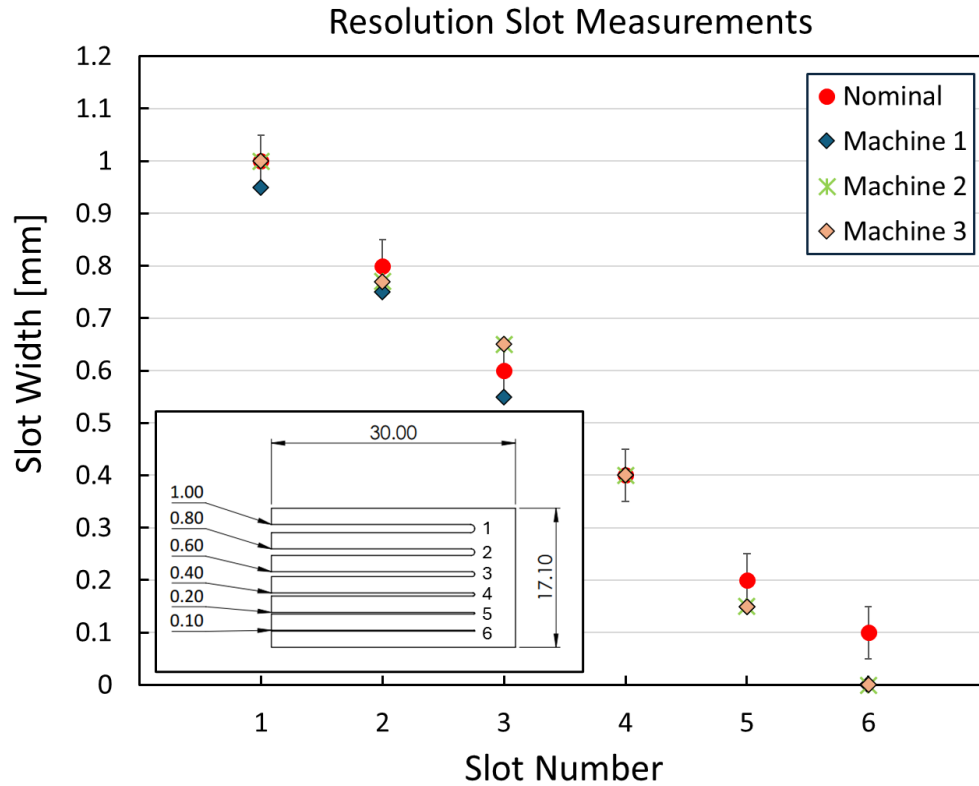


Figure 4: Resolution slot measurements for all three machines compared to the nominal designed values.

The downskin surface roughness represented by the line arithmetic mean roughness,  $R_a$ , for each machine has been provided in Figure 5. In general, a decreasing trend in  $R_a$  for increasing inclination angle can be observed which is typical of L-PBF parts [18]. Red arrows in Figure 5 point to the 30° and 45° overhang for Machine 1 which did not fabricate successfully causing significant damage to the carbon fiber brush recoater. As a result, supports were added to the 30° and 45° overhangs for Machines 2 and 3 to prevent the same occurrence (as pointed to by the blue arrows). Due to the issues in printing on Machine 1, the surface roughness for the 30° and 45° overhangs are evidently much higher than the other machines and the data points have not been included in Figure 5. However, the 60°, 75°, and 90° overhangs are comparable which provides evidence for good reproducibility in downskin surface quality. Furthermore, consistency can be observed for measurements taken using both contact and non-contact methods, i.e., profilometer for Machines 2 and 3, and optical method for Machine 1.

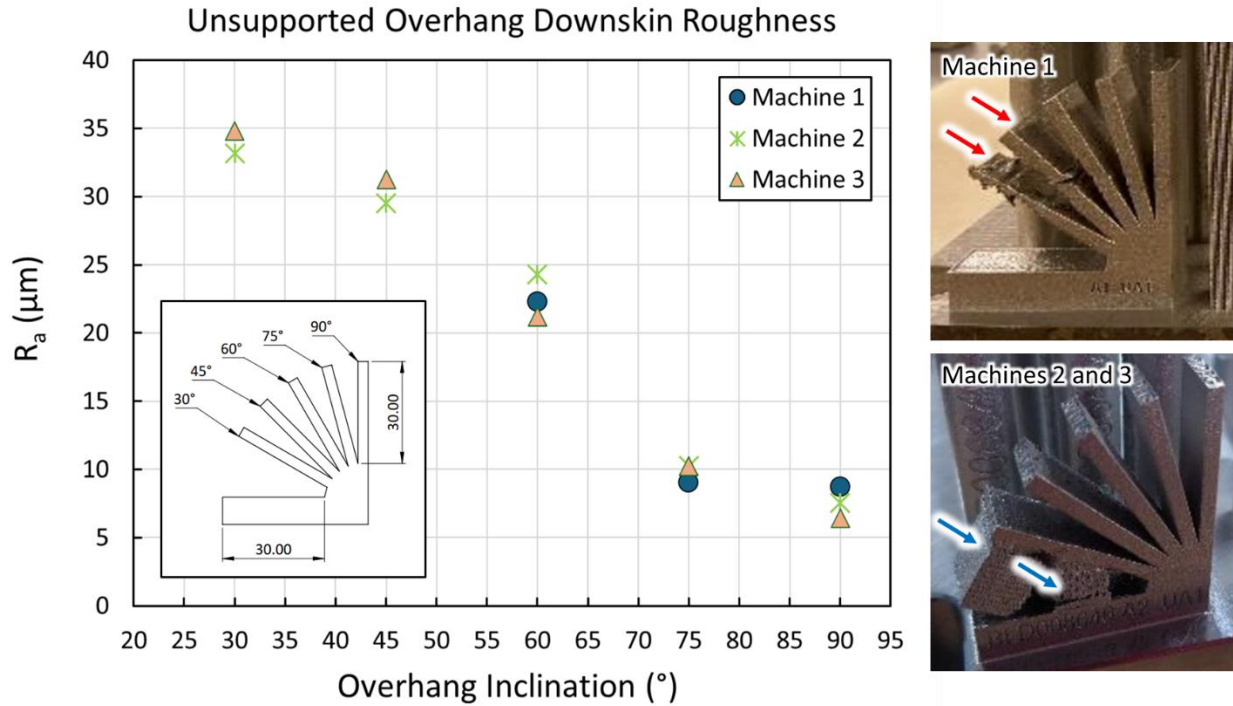


Figure 5: Downskin surface roughness results for unsupported overhangs at different inclination angles for all machines.

Chemical composition of the feedstock for each build has been provided in Table 2. Similar compositions can be observed for Machines 2 and 3 since the same virgin powder was used for fabrication. Machine 1, however, differs slightly with lower traces of Cr, Mo, and Ti, and higher Ni content. These differences can be due to the different powder suppliers used and since the powder used on Machine 1 was reused multiple times prior, resulting in minor changes in composition. However, the feedstock from each machine can be observed to comply with the limits established in ASTM F3055.

Table 2: Chemical compositions of powder feedstocks for different machines obtained from powder capsules along with the allowable minimum and maximum ranges from ASTM F3055.

Element	Machine 1	Machine 2	Machine 3	Min (ASTM F3055)	Max (ASTM F3055)
Al	0.45	0.43	0.43	0.2	0.8
B	<0.005	0.001	0.001	-	0.006
C	0.03	0.03	0.03	-	0.08
Co	0.04	<0.01	<0.01	-	1.0
Cr	18.37	19	19	17.0	21.0
Cu	0.02	0.01	<0.01	-	0.30
Fe	18.16	18.3	18.2	Bal	Bal
Mn	0.06	0.02	0.02	-	0.35
Mo	2.85	3.16	3.13	2.80	3.30
N	<0.01	N/A	N/A	N/A	N/A
Nb + Ta	4.97	5	4.99	4.75	5.50
Ni	53.93	52.97	53.14	50.0	55.00
P	<0.005	<0.005	<0.005	-	0.015
S	0.001	<0.003	<0.003	-	0.015
Si	0.02	0.004	0.004	-	0.35
Ti	0.88	1.03	1.01	0.65	1.15

The particle size distributions for the powder used on each machine are shown in Table 3. In general, a narrower size distribution can be observed for Machine 1 feedstock. This can be due to the powder reuse effect which causes powder to agglomerate [19]. The repeated sifting of powder using a mesh size of 63  $\mu\text{m}$  prevented larger particles from passing through resulting in the lower D90 value as compared to Machines 2 and 3 powders which were virgin.

Table 3: Particle size distributions for powders used on different machines.

Parameter	Machine 1	Machine 2	Machine 3
D10	25.4	18.2	18.2
D50	35.2	31.0	31.0
D90	49.2	49.7	49.7

The as-built and HT microstructure results for each machine have been provided in Figure 6. Grain size has been reported in terms of ASTM grain size number,  $G$ , according to ASTM E112 [20]. For Machine 1, average grain size was determined with the aid of EBSD and later converted to  $G$  using the conversion tables in ASTM E112 where larger  $G$  corresponds to smaller grain size. Machine 2 and 3 relied on optical images and the use of the intercept method to determine grain size of as-built material whereas the HT material was analyzed using BSE images. The grain size of the as-built microstructure obtained from Machine 1 ( $G \approx 8$  which corresponds to a grain size

of 22.5  $\mu\text{m}$ ) appears smaller than the others ( $G \approx 6.5$  which corresponds to a grain size of 37.80  $\mu\text{m}$  for Machines 2 and 3) in Figure 6a). This was likely due to the types of measurement technique used. The use of EBSD may allow for detection of very small grains which could lower the reported average grain size measurement when compared to the intercept method. Nevertheless, the morphology of the grains using both methods appears consistent. As-built microstructure of L-PBF alloys often consists of columnar grains elongated in the build direction [21]. Since coupons for Machines 2 and 3 were etched and analyzed, the melt pool boundaries can also be observed as shown in Figure 6e) and g). For simplicity, only the images taken on the XZ-plane for each machine were included in Figure 6.

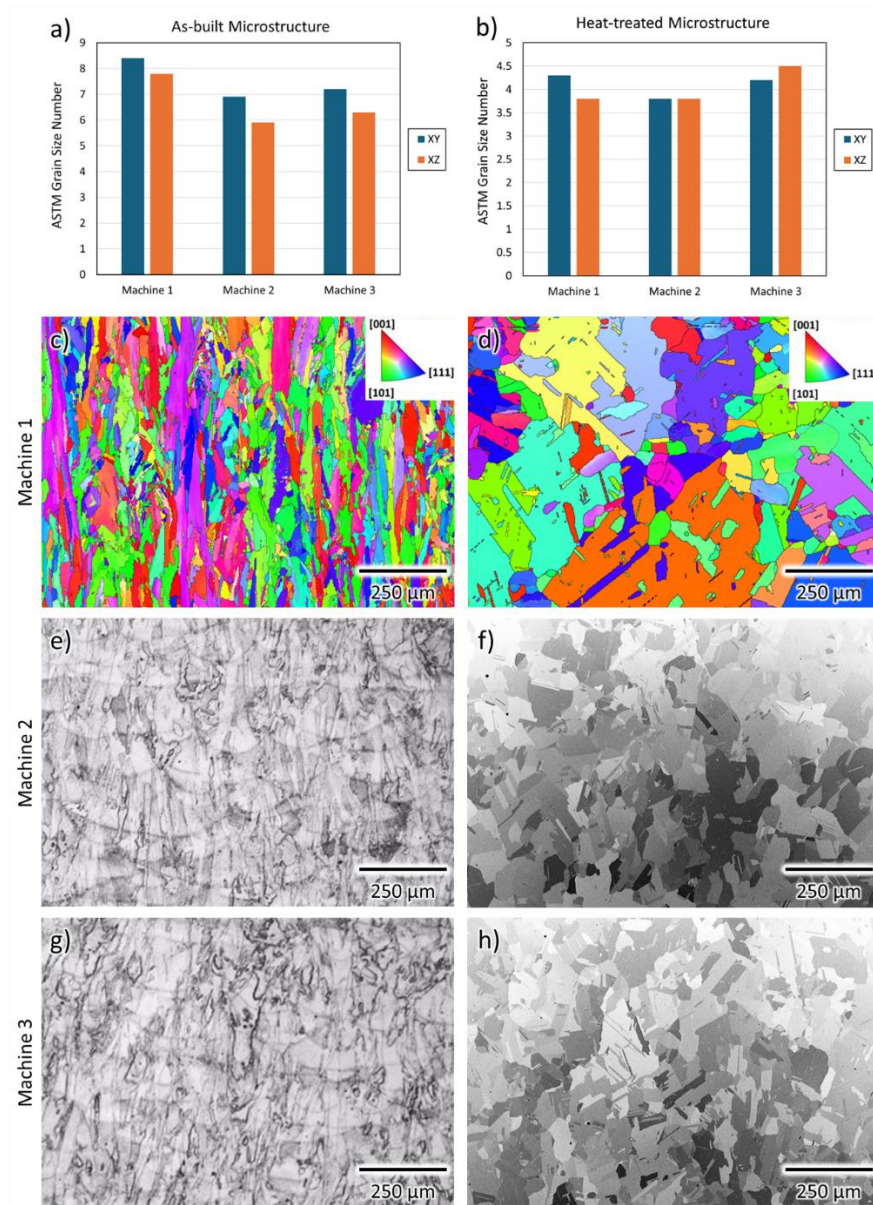


Figure 6: Grain size comparison among different machines and HT states in a) and b) along with microstructure on XZ-planes of tall cuboids in c) – h).

After HT,  $G$  can be observed to decrease significantly, i.e., increase in grain size, to  $G \approx 4$  which corresponds to a grain size of 89.80  $\mu\text{m}$ . Recrystallization and grain growth is expected in IN718 after SR, HIP, and SA at temperatures above 1065  $^{\circ}\text{C}$  [22,23]. Machine 3 microstructure possesses slightly higher  $G$  than the others which could be a result of inconsistent HT or even variations in the grain size distribution in the chosen sites for measurement. In general, the large variation observed between the two measurement techniques in as-built material is not noticeable in HT material. The grains are more regular in shape, allowing for more accurate measurements using the intercept method and also since BSE images were used for measurement which provided higher resolution compared to etched coupons.

The relative density of both the as-built and HT material is shown in Figures 7a) and b), respectively. The as-built material possessed typical process induced volumetric defects in the form of gas entrapped pores and small lack-of-fusions. On average, Machine 1 showed the highest as-built relative density whereas Machine 2 showed the lowest. All machines were up to date on maintenance therefore, machine health was not the cause of the observed difference in relative density. The likely cause may have been the different feedstocks used. Machine 1 utilized reused powder from AP&C whereas Machines 2 and 3 utilized virgin powder from Sandvik. There have been reports in literature that reusing powder can often lead to better achievable packing state compared to virgin powder as the particles become irregular in shape allowing them to fit better together than spherical ones [19]. After HT, most defects were eliminated which would have occurred during the HIP cycle. The relative density for all machines was 99.99%. Measured relative densities were not rounded up to 100% since some small defects were not completely removed during HIP.

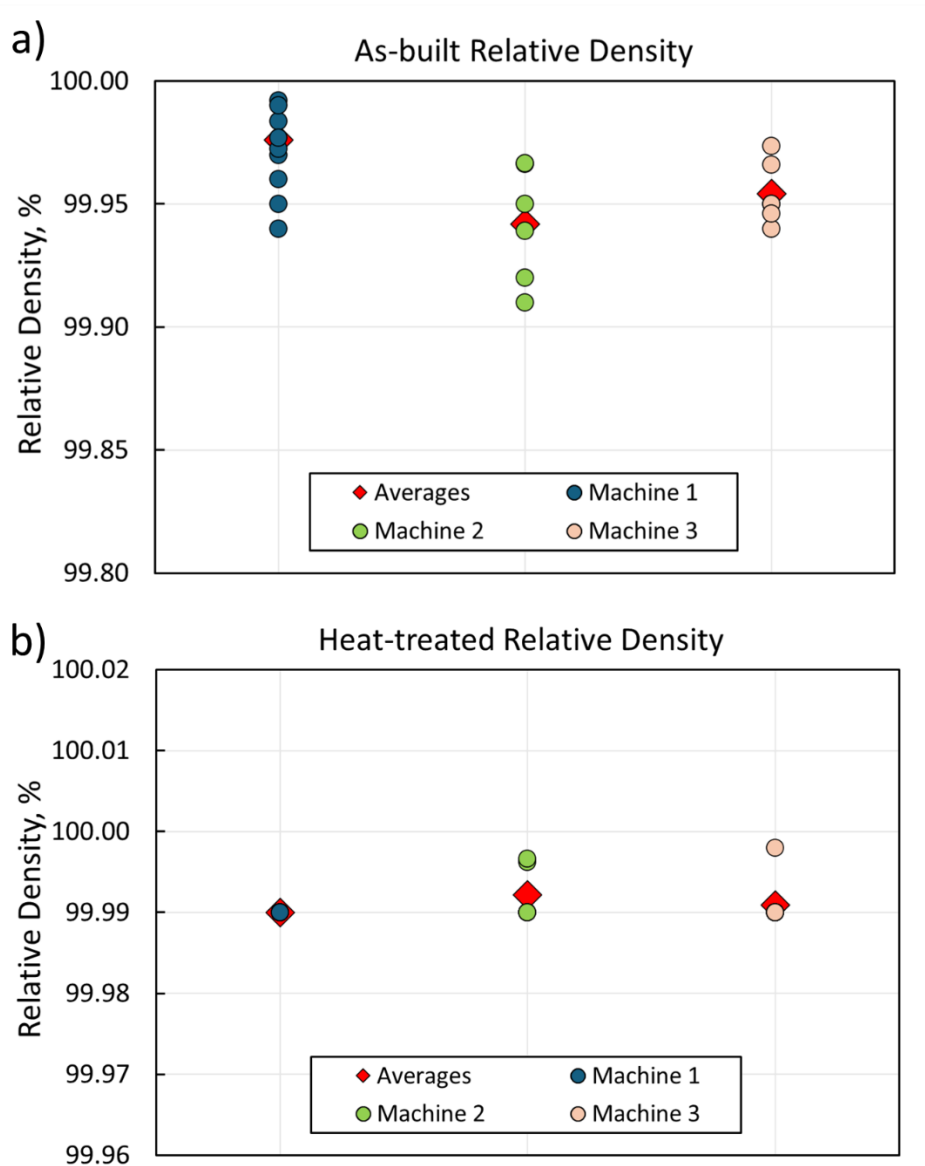


Figure 7: Relative density comparison of different machines in a) as-built and b) HT conditions.

The tensile results for each machine have been included in Figure 8. Higher yield strength,  $S_y$ , and ultimate tensile strength,  $S_u$ , can be observed for Machine 1 whereas the elongation at fracture, EL, for Machine 1 can be observed to be lower than the others. Tensile strength can often be linked to grain size; however, based on the results presented in Figure 6, grain size was comparable. Since IN718 is a  $\gamma'$  and  $\gamma''$  strengthened alloy, differences in the resulting precipitate distribution after HT may affect the strength of the material, particularly the  $S_y$ , more than differences in grain size. Precipitate distribution, however, could not be determined in this study, but since Machine 1 material was HT at a different site as Machines 2 and 3, potential for inconsistencies in the heating and cooling rates as well as the hold times during aging exist. The

average strengths, however, differed by approximately 20 MPa, which was not significant and agree with similar material available in the literature [23,24].

Elongation at fracture differs slightly for each machine, with an opposite trend to strength observed in Figure 8c). Fracture surfaces for different machines were comparable with a well-defined central region and shear lips at 45° to the fracture plane. As such, only one fracture surface was included in Figure 8d) for reference. Fracture occurred in a ductile manner leaving fine, micron-sized dimples on the fracture surface. Possible explanations for the subtle differences observed in ductility, particularly the lower ductility of Machine 1 specimens, could be the presence of secondary phases such as carbides in the material which generate stress concentrations during tensile loading and early fracture [25], or the difference in chemical composition of the feedstock resulting in lower matrix strength for Machine 1 material.

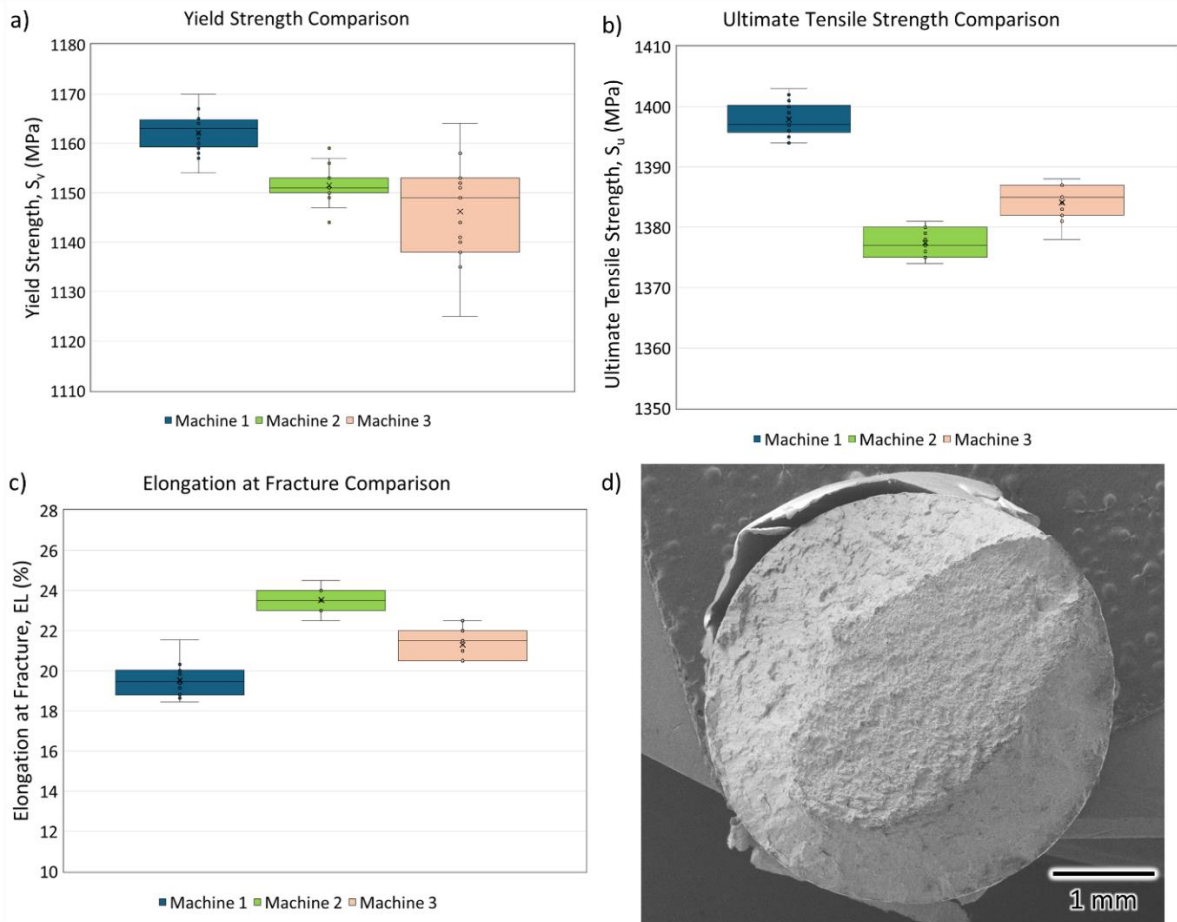


Figure 8: Comparison of tensile properties presented by box and whisker plots for different machines including a) yield strength, b) ultimate tensile strength, and c) elongation at fracture; d) a fracture surface of one tensile specimen.

The fatigue results for both LCF and HCF from each machine have been included in Figure 9a) and d), respectively. The LCF behavior is quite consistent over all machines with average

reversals to failure,  $2N_f$ , of approximately 15,000, regardless of subtle differences in chemical composition and microstructure that may occur. Analysis of the fracture surfaces for all specimens revealed multiple crack initiation sites near the surface of the specimens (top row of Figure 9). Crack initiation sites contained crystallographic facets that are indicative of the operation of persistent slip bands, typical of Ni-based superalloys [25–27]. Process induced volumetric defects, which can sometimes initiate cracks in L-PBF materials [28,29], were mostly removed during HIP therefore, none can be observed on the fracture surfaces.

Comparing the HCF results for each machine, it can be observed that there is a small separation between the specimens from Machine 1 and the other two machines. Overall, the HCF behavior of all machines appears to be comparable, however, one outlier for Machine 1 tested at 675 MPa exists. The fracture surface for this specimen has been included in Figure 9e) and f). A large crystallographic facet near the center of the specimen can be observed at the crack initiation site. Compared to other specimens, the size of this facet was much larger. Some correlations between facet size and HCF life have been explored in literature where larger facets often correlate with lower HCF life. Nevertheless, other specimens exhibited similar fracture surfaces with single initiation sites, unlike LCF specimens. Crack initiation sites were mainly near the surface of other specimens.

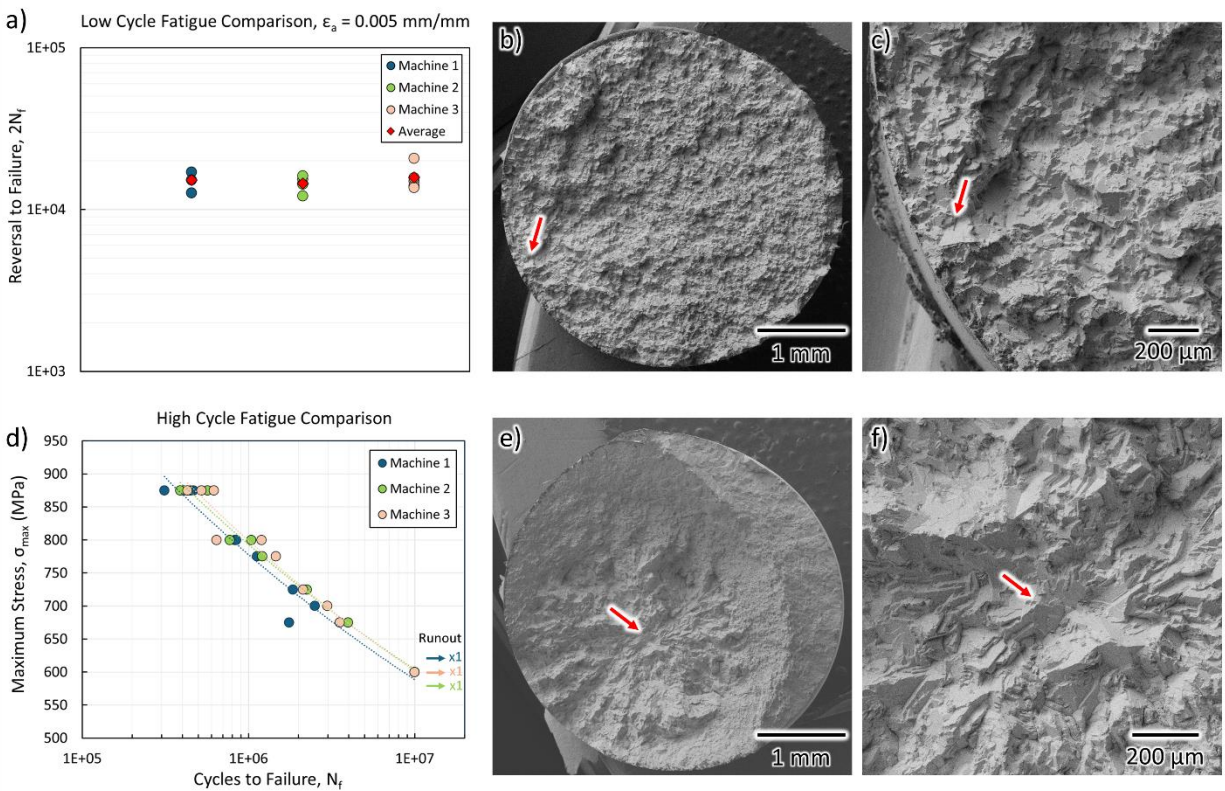


Figure 9: LCF and HCF results for different machines in a) and d), respectively. Fractography of one specimen representative of other specimens for LCF in b) and c). Fractography of the outlier HCF specimen tested at 675 MPa in e) and f). Red arrows point to crack initiation sites.

## **Conclusions**

This study assessed the reproducibility of IN718 parts on three separate EOS M290 systems through micro-/defect-structure, tensile and fatigue behavior, and dimensional accuracy. The following conclusions can be drawn from the experimental results and analyses:

1. Dimensional accuracy across all builds did not differ significantly, however, minor differences could relate to measurement techniques used and machine specific parameters such as scaling factors.
2. Microstructures across all builds were visually consistent and the observed differences in grain size were likely because of the different measurement techniques used.
3. Mechanical behavior including tensile and fatigue was comparable across all builds, however, some minor differences may have been induced by variations in heat treatment and mechanical testing at different sites.
4. Parts can be reproducible on similar L-PBF systems provided they pass all necessary qualifying checks. All differences observed may be related to testing and characterization techniques, as well as feedstock and post-processing procedures rather than machine variability.

## **Acknowledgements**

The authors acknowledge the contributions of 3T Additive Manufacturing Ltd for fabrication and testing of some of the material in this study, and Dr. Alberto Bordin (ASTM International) for his efforts in compiling test, inspection, and characterization data from all three machines used in this study.

## **References**

- [1] W.E. Frazier, Metal additive manufacturing: A review, *J Mater Eng Perform* 23 (2014) 1917–1928. <https://doi.org/10.1007/S11665-014-0958-Z>.
- [2] S. Lee, Z. Ahmadi, M. Paul, M. Mahjouri-Samani, S. Shao, N. Shamsaei, In-situ tension investigation of additively manufactured silver lines on flexible substrates, *Additive Manufacturing Letters* 7 (2023) 100171. <https://doi.org/10.1016/J.ADDLET.2023.100171>.
- [3] I. Yadroitsev, A. Du Plessis, I. Yadroitsava, Basics of laser powder bed fusion, *Fundamentals of Laser Powder Bed Fusion of Metals* (2021) 15–38. <https://doi.org/10.1016/B978-0-12-824090-8.00024-X>.
- [4] R. Singh, A. Gupta, O. Tripathi, S. Srivastava, B. Singh, A. Awasthi, S.K. Rajput, P. Sonia, P. Singhal, K.K. Saxena, Powder bed fusion process in additive manufacturing: An overview, *Mater Today Proc* 26 (2020) 3058–3070. <https://doi.org/10.1016/J.MATPR.2020.02.635>.

- [5] D. Dev Singh, T. Mahender, A. Raji Reddy, Powder bed fusion process: A brief review, *Mater Today Proc* 46 (2021) 350–355. <https://doi.org/10.1016/J.MATPR.2020.08.415>.
- [6] M. Paul, S. Soman, S. Shao, N. Shamsaei, Fatigue crack growth in L-PBF Ti-6Al-4V: Influence of notch orientation, stress ratio, and volumetric defects, *Int J Fatigue* 198 (2025) 109027. <https://doi.org/10.1016/J.IJFATIGUE.2025.109027>.
- [7] P.J. Wilson, E. Azizian-Farsani, M. Paul, M.M. Khonsari, S. Shao, N. Shamsaei, On the damping and fatigue characterization of additively manufactured Ti-6Al-4V, *Additive Manufacturing Letters* 11 (2024) 100260. <https://doi.org/10.1016/j.addlet.2024.100260>.
- [8] M. Salman Yasin, A. Soltani-Tehrani, A. Poudel, S. Shao, N. Shamsaei, Key process variable (KPV) variations and their impact on defect structure and tensile behavior of L-PBF Ti-6Al-4V, n.d.
- [9] F. Calignano, M. Galati, L. Iuliano, A Metal Powder Bed Fusion Process in Industry: Qualification Considerations, *Machines* 2019, Vol. 7, Page 72 7 (2019) 72. <https://doi.org/10.3390/MACHINES7040072>.
- [10] ASTM International, Additive manufacturing-Qualification principles-Installation, operation and performance (IQ/OQ/PQ) of PBF-LB equipment, n.d. <https://www.iso.org/obp>.
- [11] E. Maleki, B. Salehnasab, M. Paul, S. Shao, N. Shamsaei, Dimensional accuracy of fabricated geometries through powder bed fusion: An overview and a new benchmark artifact proposal, *Mater Des* 257 (2025) 114361. <https://doi.org/10.1016/J.MATDES.2025.114361>.
- [12] E. Hosseini, V.A. Popovich, A review of mechanical properties of additively manufactured Inconel 718, *Addit Manuf* 30 (2019) 100877. <https://doi.org/10.1016/j.addma.2019.100877>.
- [13] I. Nandi, N. Shamsaei, S. Shao, Investigating the effect of defects on the crack initiation of additively manufactured IN718 using crystal plasticity simulations, (2022). <https://doi.org/http://dx.doi.org/10.26153/tsw/44170>.
- [14] ASTM E8/E8M, Standard Test Method for Tension Testing of Metallic Materials, American Society for Testing and Materials (2013) 1–28.
- [15] ASTM International, Strain-Controlled Fatigue Testing, ASTM Standards, E606 92 (2013) 1–16.
- [16] ASTM International, Practice for Conducting Force Controlled Constant Amplitude Axial Fatigue Tests of Metallic Materials, (2015). <https://doi.org/10.1520/E0466-15>.

- [17] ISO/ASTM 52902:2023 - Additive manufacturing — Test artefacts — Geometric capability assessment of additive manufacturing systems, (n.d.). <https://www.iso.org/standard/79683.html> (accessed May 23, 2025).
- [18] J. Elambasseril, J. Rogers, C. Wallbrink, D. Munk, M. Leary, M. Qian, Laser powder bed fusion additive manufacturing (LPBF-AM): the influence of design features and LPBF variables on surface topography and effect on fatigue properties, *Critical Reviews in Solid State and Materials Sciences* 48 (2023) 132–168. <https://doi.org/10.1080/10408436.2022.2041396>.
- [19] A. Soltani-Tehrani, J.P. Isaac, H. V. Tippur, D.F. Silva, S. Shao, N. Shamsaei, Ti-6Al-4V powder reuse in laser powder bed fusion (L-PBF): The effect on porosity, microstructure, and mechanical behavior, *Int J Fatigue* 167 (2023) 107343. <https://doi.org/10.1016/J.IJFATIGUE.2022.107343>.
- [20] ASTM International, Test Methods for Determining Average Grain Size, (2021). <https://doi.org/10.1520/E0112-13R21>.
- [21] Z. Wang, K. Guan, M. Gao, X. Li, X. Chen, X. Zeng, The microstructure and mechanical properties of deposited-IN718 by selective laser melting, *J Alloys Compd* 513 (2012) 518–523. <https://doi.org/10.1016/j.jallcom.2011.10.107>.
- [22] K. Gruber, W. Stopyra, K. Kobiela, B. Madejski, M. Malicki, T. Kurzynowski, Mechanical properties of Inconel 718 additively manufactured by laser powder bed fusion after industrial high-temperature heat treatment, *J Manuf Process* 73 (2022) 642–659. <https://doi.org/10.1016/J.JMAPRO.2021.11.053>.
- [23] N. Ahmad, R. Ghiaasiaan, P.R. Gradl, S. Shao, N. Shamsaei, Revealing deformation mechanisms in additively manufactured Alloy 718: Cryogenic to elevated temperatures, *Materials Science and Engineering: A* 849 (2022) 143528. <https://doi.org/10.1016/J.MSEA.2022.143528>.
- [24] N. Ahmad, A. Bidar, R. Ghiaasiaan, P.R. Gradl, S. Shao, N. Shamsaei, A Comparison of Microstructure and Mechanical Performance of Inconel 718 Manufactured via L-PBF, LP-DED, and WAAM Technologies, (2023). <https://doi.org/https://doi.org/10.26153/tsw/50937>.
- [25] M. Paul, R. Ghiaasiaan, P. Gradl, J. Caron, P. Wang, S. Shao, N. Shamsaei, Tensile and fatigue behaviors of newly developed HAYNES® 233 alloy: Additively manufactured vs. wrought, *Mater Des* 244 (2024) 113165. <https://doi.org/10.1016/J.MATDES.2024.113165>.
- [26] P. Lukáš, L. Kunz ‡, Role of persistent slip bands in fatigue, *Philosophical Magazine* 84 (2004) 317–330. <https://doi.org/10.1080/14786430310001610339>.

- [27] M.S. Dodaran, M. Muhammad, N. Shamsaei, S. Shao, Synergistic effect of microstructure and defects on the initiation of fatigue cracks in additively manufactured Inconel 718, *Int J Fatigue* 162 (2022) 107002. <https://doi.org/10.1016/j.ijfatigue.2022.107002>.
- [28] S. Tammis-Williams, P.J. Withers, I. Todd, P.B. Prangnell, The Influence of Porosity on Fatigue Crack Initiation in Additively Manufactured Titanium Components, *Scientific Reports* 2017 7:1 7 (2017) 1–13. <https://doi.org/10.1038/s41598-017-06504-5>.
- [29] K. Yang, Q. Huang, Q. Wang, Q. Chen, Competing crack initiation behaviors of a laser additively manufactured nickel-based superalloy in high and very high cycle fatigue regimes, *Int J Fatigue* 136 (2020) 105580. <https://doi.org/10.1016/J.IJFATIGUE.2020.105580>.